Evolution of the microstructure, texture and creep properties of the 7075 aluminium alloy during hot accumulative roll bonding

P. Hidalgo-Manrique[1],*, C.M. Cepeda-Jiménez[1], A. Orozco-Caballero, O.A. Ruano, F. Carreño

Department of Physical Metallurgy, CENIM, CSIC, Av. Gregorio del Amo 8, 28040 Madrid, Spain

[1]*Present address: IMDEA Materials Institute, C/Eric Kandel 2, 28906 Getafe, Madrid, Spain*

*Corresponding author: Tel.: +34 91 549 34 22; e-mail address: paloma.hidalgo@imdea.org

Abstract

The 7075 Al alloy was severely deformed at 350ºC by a 3:1 thickness reduction per pass accumulative roll bonding (ARB) process up to six passes. It was found that discontinuous recrystallization occurs during the inter-pass annealing stages from the third pass on, attributable to the increment of the mean particle size during processing. As a consequence, the mean crystallite size did not decrease, but remained approximately constant at 440 nm along the present ARB process and the mean boundary misorientation angle reached a maximum of 30º for the 3-passes sample. However, since nucleation of new grains takes place at the pre-existing grain boundaries, discontinuous recrystallization results in slight changes in texture throughout the processing, being the orientations in the ARBed samples predominantly located along the typical rolling β-fibre. Uniaxial tests conducted at 300ºC and 350ºC revealed that the operating deformation mechanism in the processed alloy at such temperatures was grain boundary sliding, the optimum superplastic strain rate being $3 \cdot 10^{-3}$-10^{-2} s^{-1}. Boundary misorientation and thermal stability are the two main factors that contribute to high elongations to failure.

1. Introduction

Accumulative roll bonding (ARB) is a severe plastic deformation process developed in 1998 by Saito et al. [1], consisting of multiple cycles of cutting, stacking and roll bonding. So, large strains can be accumulated in the material and significant structural refinement can be achieved [2]. Since 1998, extensive studies regarding the evolution of microstructure during ARB have been conducted [3-9]. According to these studies, grain refinement takes place in a gradual manner which can be characterized as continuous recrystallization. In the particular case of aluminium, studies on the microstructural evolution during ARB have been widely performed on pure aluminium [6] and several alloys such as AA3003 [5], AA6061 [4] and AA8006 [8], while a few studies have been performed on the aeronautical 7075 Al alloy [10-12], despite the large advantages that would arise from refining its microstructure. A previous work [10] revealed that, as a high-strength alloy, the 7075 Al alloy needs to be processed at a minimum temperature of 300ºC in order to attain sufficient bonding and good workability. However, it must be taken into account that this alloy contains thermally unstable precipitates [13,14], which for certain processing temperature may alter or hinder the expected grain refinement process.

Although extensive studies have been conducted regarding the microstructural evolution during ARB, there is only limited quantitative information available on the texture evolution during this process [15-18], despite the fact that the texture affects the ductility and the mechanical anisotropy which, in turn, determine the material formability. Moreover, texture measurements during ARB have been made after the roll-bonding steps, but never after the inter-pass heating stages, where significant texture changes may take place as a

consequence of certain restoration processes, such as discontinuous recrystallization [12]. That is, no studies on the influence of the inter-pass heating stages on the texture evolution have been performed. Several works revealed that the texture developed by ARB in the mid-thickness regions of the samples is very similar to that developed by conventional rolling and, as such, it is characterized by rolling-type components. However, textures developed by ARB are normally weaker [1,6,19] and even less symmetric [1]. In order to understand these differences it must be considered that shear strain is introduced into the sample surface during any rolling process due to the large friction between the rolls and the sample. Consequently, the surface regions of the rolled samples exhibit shear texture. In the ARB process, upon cutting and stacking steps, surface regions are transferred into the sample interior. The introduction of shear strain may alter the slip pattern from that which characterizes conventional rolling. Additionally, although shear texture is easily destroyed, the introduction of shear orientations may retard the development of a strong rolling texture.

The superplastic forming (SPF) technology has already found numerous industrial applications, as it can be used to fabricate components with a complex shape and uniform thickness in a single forming operation. This procedure eliminates the need for the assembly of separately made parts and leads to a reduction of tooling costs [20]. The underlying basis for SPF is superplasticity, characterized by enhanced ductility and low stress, operating through the so-called grain boundary sliding (GBS) creep mechanism [21,22]. In high strength aluminium alloys, such as 7075, superplasticity has been traditionally developed by complex thermomechanical processes [23-27]. The resulting materials with a grain size around 10 μm exhibited optimum superplasticity at temperatures close to 500ºC and at strain rates of the order of 10^{-4} s^{-1}. These conditions lead to so elevated costs which necessarily confine the applications of SPF to low-volume production. Experiments [28,29] show that a shift to lower deformation temperatures and/or higher strain rates can be attained by further

grain refinement. Thus, ARB gives the opportunity to make SPF cost-effective, extending its commercial application.

In the present work, the 7075-T6 Al alloy was deformed at 350ºC by a 3:1 thickness reduction per pass ARB process up to six passes. The evolution of the microstructure, texture and creep properties was carefully examined. Moreover, the superplastic behaviour of the processed alloy at temperatures lower and strain rates higher than conventional for optimum superplasticity was evaluated.

2. Material and experimental procedure

The material used for the present work was a 2 mm-thick sheet of the commercial 7075 aluminium alloy in the T6 condition. The chemical composition is shown in Table 1. Microstructural examinations showed a microstructure composed of pancake-shaped grains of dimensions 60 x 47 x 4 μm^3. The orientations characterization showed a pronounced cube texture with rolling direction-scatter [11].

From the as-received alloy sheet two pieces with dimensions 2 mm x 30 mm x 180 mm were cut, cleaned with methyl ethyl ketone, put one on top of the other and fastened by steel wires. The resulting 4 mm-thick specimen was held for 5 minutes at 350ºC in a preheated electric furnace and straight afterwards undergone a thickness reduction of 3:1, equivalent to a true strain of 1.1, by a single rolling pass. True strain (ε) was calculated as -ln(h_0/h), where h_0 and h are the initial and the final thicknesses of the rolled specimen, respectively. Rolling was performed in non-lubricated conditions using a two-high mill with a roll diameter of 131 mm and a peripheral roll speed of 346 mm/s. Immediately after rolling, the resulting 1.33 mm-thick specimen was water quenched. Afterwards, it was divided in three identical pieces that were supplied to the next ARB pass. From that moment on, the procedure described above was executed 5 more times maintaining the rolling direction (RD).

Table 1. Chemical composition of the 7075 aluminium alloy studied (mass%).

Si	Mg	Fe	Zn	Cu	Ti	Cr	Mn	Al
0.052	2.51	0.19	5.68	1.59	0.025	0.19	0.007	bal.

The microstructures of the ARBed samples were characterized on the rolling plane in a section located at a depth of 40% from the surface by transmission electron microscopy (TEM) and electron backscatter diffraction (EBSD). The TEM studies were carried out in a JEOL JEM 2000 FX II microscope operating at 200 kV. The mean crystallite size (d) was directly calculated from the TEM micrographs as the mean boundary spacing. In this work, the term crystallite is used to describe volumes separated from the neighbouring volumes by boundaries of any misorientation angle. For TEM investigations disks of 3 mm diameter extracted from the ARBed samples were thinned to perforation using a twin-jet electropolishing facility with a solution of 30% nitric acid and 70% methanol at 15 V and -25ºC.

The EBSD mapping was conducted in a JEOL JSM 6500 F field emission gun scanning electron microscope operating at 20 kV with a working distance of 15 mm and a step size of 80 nm. Data acquisition and analysis were performed using the commercial Channel 5 software. Because of the limited angular resolution of the EBSD system, misorientations below or equal to 2º were neglected. Boundaries with misorientations from 2º to 15º were defined as low angle boundaries (LABs), while those with misorientations greater than 15º were defined as high angle boundaries (HABs). The mean boundary misorientation angle (θ) was calculated from the EBSD data. In addition, the mean spacing of HABs (d_{HAB}) was determined from the maps as mean linear intercepts along the transversal direction (TD). Specimens for EBSD investigations were mechanically ground and polished and then electropolished in the preceding solution at 15 V and -15ºC.

Textures of the ARBed samples were determined by X-ray diffraction (XRD) in a section located at a depth of 40% from the surface. The (111), (200) and (220) pole figures

were measured using CuK_α radiation in a Siemens D500 diffractometer equipped with an open Euler ring working with Schultz geometry. From these experimental pole figures and using the TexTools software the orientation distribution functions (ODFs) were derived by means of the series expansion method. The ODFs were represented in the form of sections through the Euler space, which due to the cubic crystal symmetry and the orthotropic sample symmetry is defined by $0^\circ \leq \varphi_1, \Phi, \varphi_2 \leq 90^\circ$. In particular, equal distance sections along the φ_2 angle in 5° steps are used.

Tensile dogbone specimens with gauge length of 10 mm and width of 3 mm were electro-discharge machined from the as-received sheet and the ARBed samples with their tensile axis perpendicular to the rolling direction (RD). Uniaxial tensile test to failure were conducted at 300ºC and 350ºC using a Servosis ME 405/10 and an Instron 1362 testing machine and an elliptical furnace provided with four quartz lamps in air. The tensile specimens were held at the testing temperature for 20 min before the tests and water quenched immediately after the tests. A set of tensile tests was performed at a constant crosshead speed corresponding to the initial strain rate of 10^{-2} s^{-1}. Note that initial strain rate is given by v/l_0, where v is the crosshead speed, which can be measured with high accuracy, and l_0 is the initial specimen gauge length. Yield stress ($\sigma_{0.2}$) and elongation to failure (e_F) were determined from the true stress (σ)-true strain (ε) curves. Another set of tensile tests was performed using the strain rate change (SRC) method. First, the initial strain rate is consecutively reduced in several steps from 10^{-1} s^{-1} to 10^{-5} s^{-1} utilizing constant crosshead speeds. Then, the strain rate is consecutively increased from the lowest strain rate, in several steps up to 10^{-2} s^{-1}, also utilizing constant crosshead-speeds. From the SRC tests the true strain rate ($\dot{\varepsilon}$)-true stress (σ) pairs corresponding to the decreasing strain rate steps were extracted in the steady state. As the calculations take into account the increasing specimen gauge length during testing, the accuracy of the $\dot{\varepsilon}$-σ data pairs is maximized. Using these data, the apparent stress exponent

(n_{ap}) was determined as the slope of the $\dot{\varepsilon}$-σ curves at a given temperature (T) by the following expression:

$$n_{ap} = \left.\frac{\partial \ln \dot{\varepsilon}}{\partial \ln \sigma}\right|_T$$

After the tests, the surface of the gauge sections were examined in a HITACHI S 4800 cold FEG-SEM, while the grip sections were characterized by XRD in a section located at a depth of 40% from the surface.

3. Results

Fig. 1 shows the TEM micrographs of the ARBed samples. The associated selected area electron diffraction (SAED) patterns taken from the centre of the field using the largest aperture are also shown. The 1-pass sample (Fig. 1a) exhibits a cell structure with a high dislocation density in the cell interiors and dislocation-tangling zones. Accordingly, the SAED pattern is a single net pattern. In the 2-passes sample (Fig. 1b) clear boundaries are present and dislocation density is much lower than in the 1-pass sample. In the 3-passes sample (Fig. 1c) small crystallites surrounded by well-defined boundaries with a low dislocation density are clearly seen. The SAED pattern has numerous reflections along circles, indicating that large misorientations exist between individual crystallites. It is odd that the 4-passes (Fig. 1d), 5-passes (Fig. 1e) and 6-passes (Fig. 1f) samples generally exhibit more diffused boundaries than the 3-passes sample, especially the 4-passes and the 6-passes samples. This is consistent with the reduction in spot scattering of the SAED patterns from the 3-passes sample to the 6-passes sample. Moreover, dislocation density in these samples is very high relative to that in the 3-passes sample, especially in the 4-passes and the 6-passes samples. Therefore, during the first three passes, as N increases, the dislocation density decreases and the boundary misorientation increase.
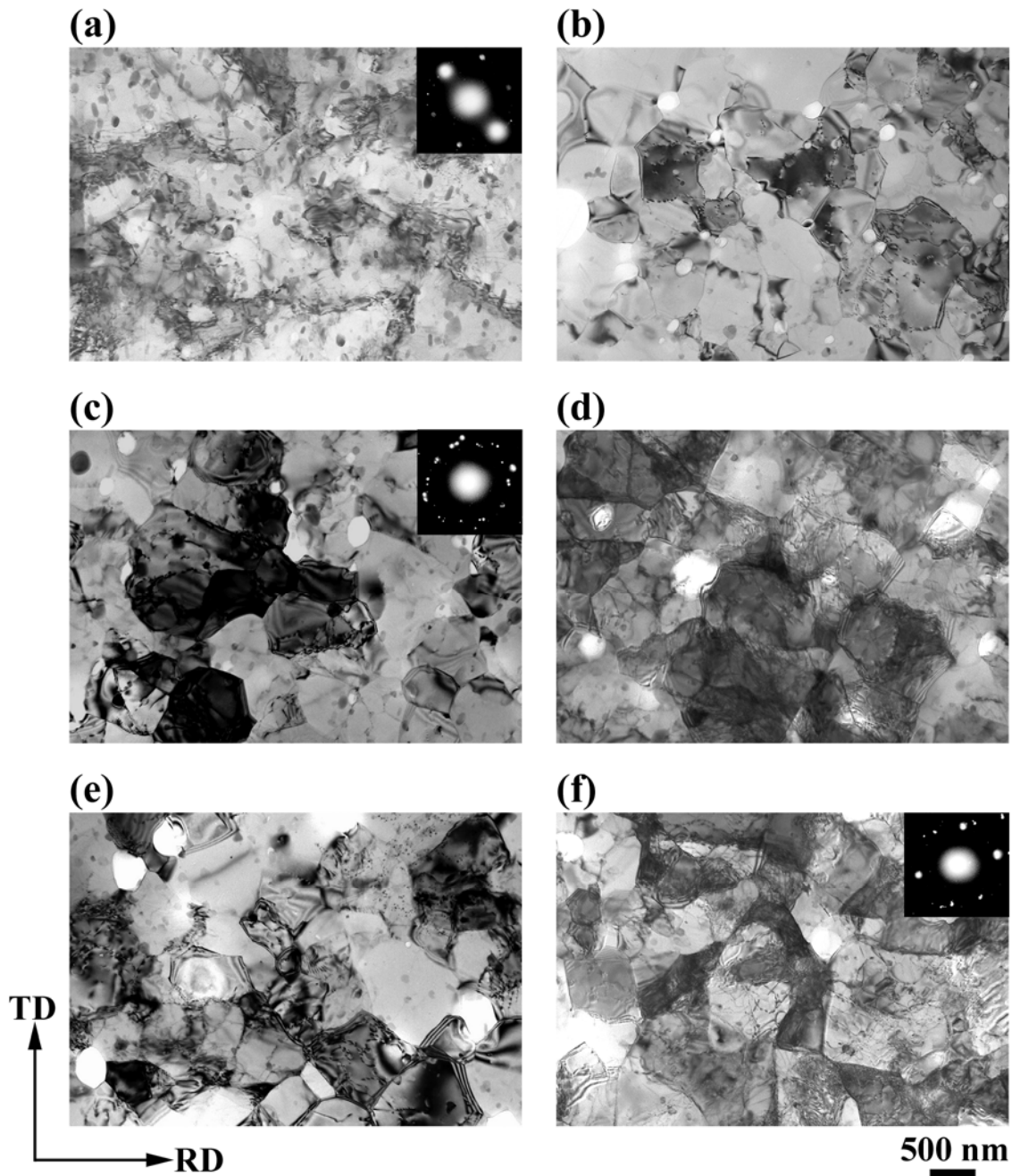
Figure 1. TEM micrographs and SAED patterns of the ARBed samples. (a) 1-pass, (b) 2-passes, (c) 3-passes, (d) 4-passes, (e) 5-passes and (f) 6-passes.

TEM micrographs in Fig. 1 also reveal an inhomogeneous particle size distribution in the ARBed samples. On the basis of previous works [12,14], the small black particles are identified as dispersoids ($Al_{12}Mg_2Cr$, $Al_{18}Mg_3Cr_2$), while the large white particles are identified as the precipitates related to the age hardening phases ($MgZn_2$, $CuMgAl_2$). Note that the Cr-rich dispersoid particles, very thermally stable [13], remain almost unchanged with increasing N. However, the Mg-Zn rich particles gradually coarsen with increasing N.

Moreover, the Mg-Zn rich particles extraordinarily coarsen from the starting material, in the T6 temper condition, where they are only some nanometers in size [26].

Fig. 2 illustrates the variation of d with N. Although it is somewhat higher for the 6-passes sample, it can be concluded that the mean crystallite size is about constant, at 440 nm, with the number of passes.

The EBSD maps of the ARBed samples are displayed in Fig. 3. The colours in the maps represent the crystallographic directions parallel to the normal direction (ND) of the samples. The correspondence between the colours and the crystallographic directions is indicated in the standard stereographic triangle shown in the picture. The non-indexed points are shown as black pixels. The LABs are depicted as grey lines, while HABs are depicted as black lines. The 1-pass sample (Fig. 3a) mainly comprises boundaries with misorientation below 2º, which fits a cell structure. The 2-passes (Fig. 3b) and the 3-passes (Fig. 3c) samples comprise LABs and HABs, compatible with a (sub)grain structure. However, the relatively large quantity of grey lines fragments in Fig. 3b reveal that the 2-passes sample still contains some cell walls. Unexpectedly, the 4-passes (Fig. 3d), 5-passes (Fig. 3e) and 6-passes (Fig. 3f) samples exhibit a fraction of HABs lower than the 3-passes sample, especially the 4-passes and the 6-passes samples. Moreover, these last two samples again exhibit a large amount of boundaries with misorientation below 2º.
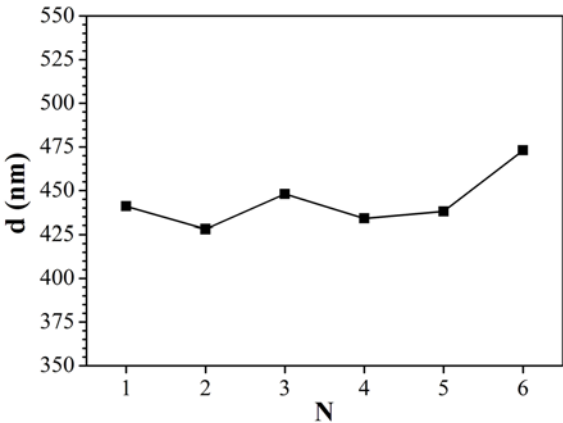

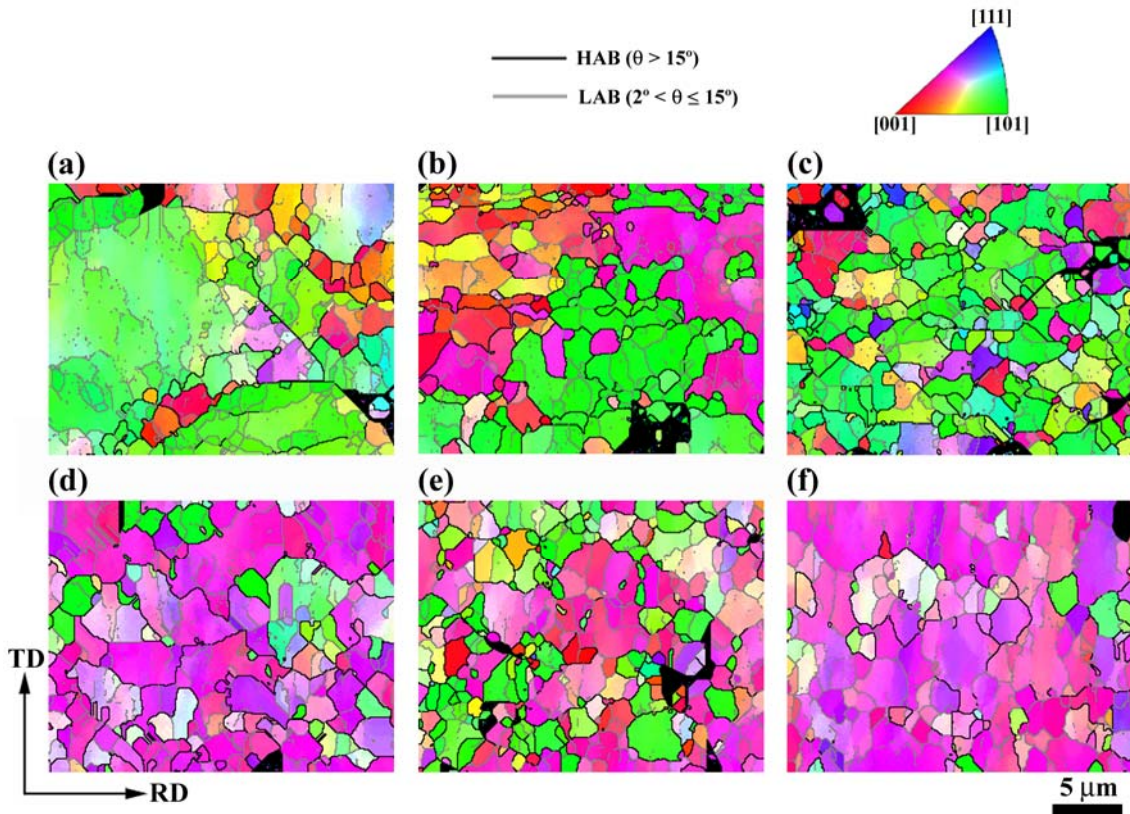**Figure 2.** Mean crystallite size (d) as a function of the number of ARB passes (N).

Figure 3. EBSD maps of the ARBed samples. (a) 1-pass, (b) 2-passes, (c) 3-passes, (d) 4-passes, (e) 5-passes and (f) 6-passes.

Fig. 4 illustrates the variation of the microstructural parameters determined from the EBSD data with N. Fig. 4a shows that θ exhibits a maximum of 30º for N = 3. It should be remembered that misorientation angles less than 2º were not included in the EBSD analysis.
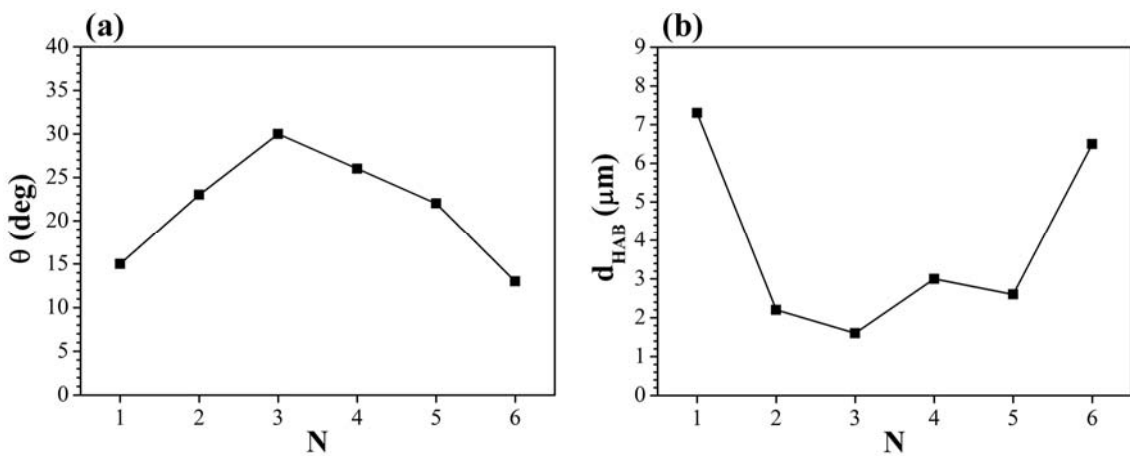

Figure 4. Microstructural parameters determined from the EBSD data as a function of the number of ARB passes, N. (a) Mean boundary misorientation angle, θ, and (b) mean spacing of high angle boundaries, d_{HAB}.

Therefore, this measure overestimates the true mean boundary misorientation angle of the ARBed samples, particularly for those samples which contain a large fraction of boundaries with misorientation below 2º [30]. In this way, for example, although θ is higher for N = 4 than for N = 5, the microstructure of the 4-passes sample is less misoriented than that of the 5-passes sample, according to the maps (Fig. 3d,e). On the other hand, Fig. 4b shows that during the first three passes d_{HAB} decreases with increasing N, reaching a value of 1.6 μm for N = 3. However, for the 4-passes, 5-passes and 6-passes samples d_{HAB} is higher than for the 3-passes sample, especially for the 6-passes one. Note that the 4-passes and the 5-passes samples exhibit similar d_{HAB}, although it is a bit smaller for the latter. Also note that the evolutions of θ and d_{HAB} with N are opposite.

The ODFs of the ARBed samples are shown in Fig. 5. The 1-pass (Fig. 5a), 3-passes (Fig. 5b) and 5-passes (Fig. 5c) samples exhibit a rolling β-fibre extending from the brass (B) orientation $(\varphi_1, \Phi, \varphi_2) = (35º, 45º, 90º)$ to the Dillamore (D) orientation $(\varphi_1, \Phi, \varphi_2) = (90º, 27º, 45º)$ passing through the S orientation $(\varphi_1, \Phi, \varphi_2) = (59º, 37º, 63º)$. The 1-pass sample also exhibits cube (C) orientation $(\varphi_1, \Phi, \varphi_2) = (0º, 0º, 0º)$ and the rotations of this orientation along the RD, which were retained from the initial texture. A more detailed examination of the textures
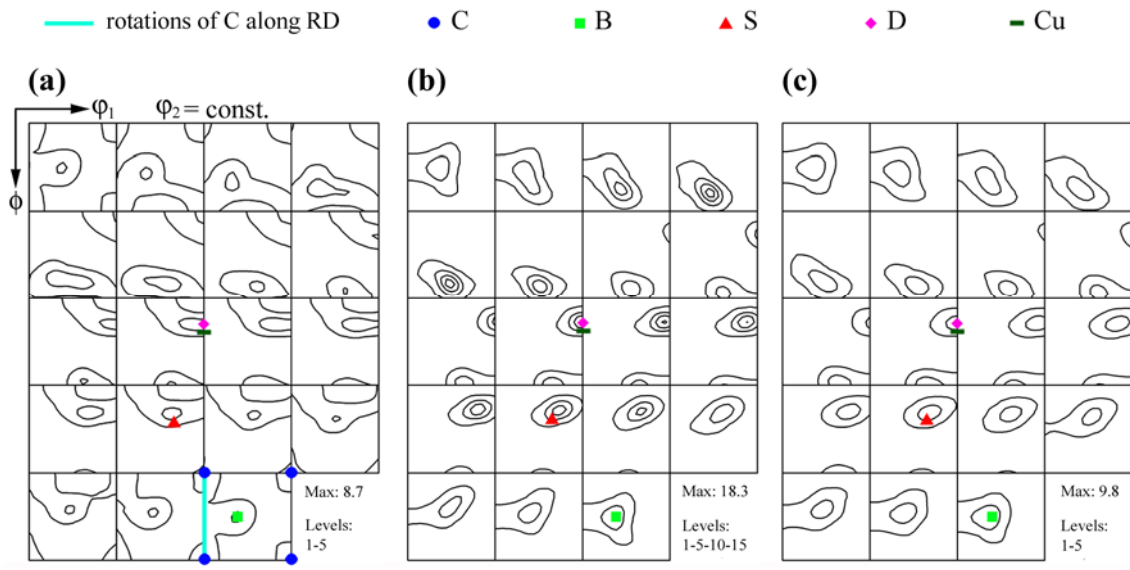

Figure 5. ODFs of the ARBed samples. (a) 1-pass, (b) 3-passes and (c) 5-passes.

reveals that for the 1-pass and the 5-passes samples the orientations along the β-fibre are uniformly distributed. However, for the 3-passes sample, which exhibits the highest intensity, the fraction of orientations along the β-fibre gradually increases from B to D.

Fig. 6 represents the tensile properties at 300ºC and 350ºC and at an initial strain rate of 10^{-2} s^{-1} as a function of N. Fig. 6a shows that, at 300ºC, $\sigma_{0.2}$ gradually decreases from 109 MPa for the as-received material to 49 MPa for the 3-passes sample, but then gradually increases up to 60 MPa for the 6-passes sample. Similarly, at 350ºC, $\sigma_{0.2}$ gradually decreases from 60 MPa for the as-received material to 33 MPa for the 4-passes sample, but then raises up to 46 MPa for the 6-passes sample. That is, the evolution of $\sigma_{0.2}$ with N exhibits a minimum. However, at 300ºC it is located at N = 3, while at 350ºC it is at N = 4. As it will be discussed later, this behaviour is related to thermal stability. Fig. 6b shows that e_F is higher for the ARBed samples than for as-received material. Initially, e_F progressively increases with N, reaching a value of 140% for N = 3 at 300ºC and a value of 185% for N = 4 at 350ºC, but then it drops for N = 6.

The $\dot{\varepsilon}$-σ data obtained during the SRC tests at 300ºC and 350ºC for the as-received material and the ARBed samples are represented in a double logarithmic scale in Fig. 7. The n_{ap} values represented in the figure correspond to the as-received material and to the least
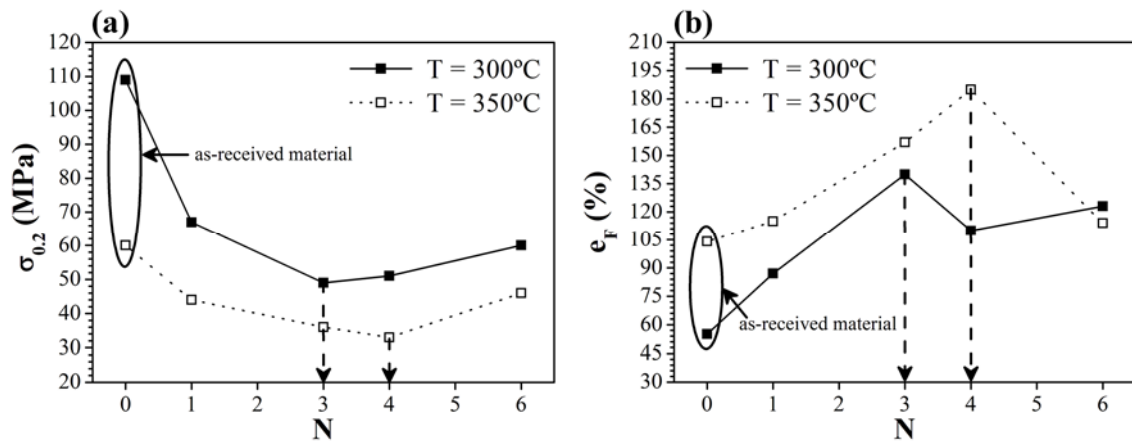

Figure 6. Tensile properties at 300ºC and 350ºC and at an initial strain rate of 10^{-2} s^{-1} as a function of the number of ARB passes, N. (a) Yield stress, $\sigma_{0.2}$, and (b) elongation to failure, e_F.
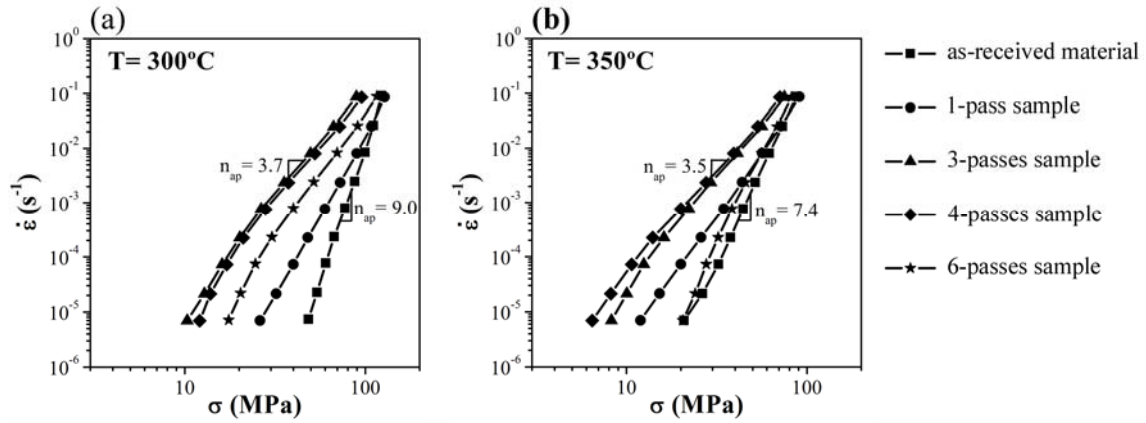
Figure 7. Dependence of the true strain rate, $\dot{\varepsilon}$, on the true stress, σ, for the as-received material and the ARBed samples. (a) When testing at 300°C and (b) when testing at 350°C. The apparent stress exponents, n_{ap}, of the as-received sample and the softest ARBed sample at each testing temperature are included.

creep resistant ARBed sample at each testing temperature. It is clear that the ARBed samples show lower flow stresses than the as-received sample. Moreover, the curves of the ARBed samples display lower slopes than those of the as-received material, especially at the intermediate-high strain rates. Fig. 7a reveals that, at 300°C, the $\dot{\varepsilon}$-σ curves gradually shift to lower creep stresses with increasing N up to N = 3, but then shift to higher stresses with increasing N. That is, at 300°C the lowest flow stresses correspond to the 3-passes sample, exhibiting a minimum value of n_{ap}= 3.7 between $3 \cdot 10^{-3}$ s^{-1} and 10^{-2} s^{-1}, while the as-received material exhibits a value of n_{ap}= 9.0 in the vicinity of 10^{-3} s^{-1}. Similarly, Fig. 7b reveals that, at 350°C, the $\dot{\varepsilon}$-σ curves gradually shift to lower creep stresses with increasing N up to N = 4, but then shift to higher stresses with increasing N. That is, at 350°C, the lowest flow stresses correspond to the 4-passes sample, exhibiting a minimum value of n_{ap}= 3.5 between $3 \cdot 10^{-3}$ s^{-1} and 10^{-2} s^{-1}, while the as-received material exhibits a value of n_{ap}= 7.4 in the same interval.

Fig. 8 shows SEM images taken from the surface of gauge sections after testing at an initial strain rate of 10^{-2} s^{-1}. Fig. 8a corresponds to the 3-passes sample tested at 300°C, while Fig. 8b corresponds to the 4-passes sample tested at 350°C. In both cases a homogeneous microstructure composed of fairly equiaxed crystallites of ~ 2 μm in diameter is present. It is clear that the microstructures of both ARBed samples coarsen during the tests. However, the
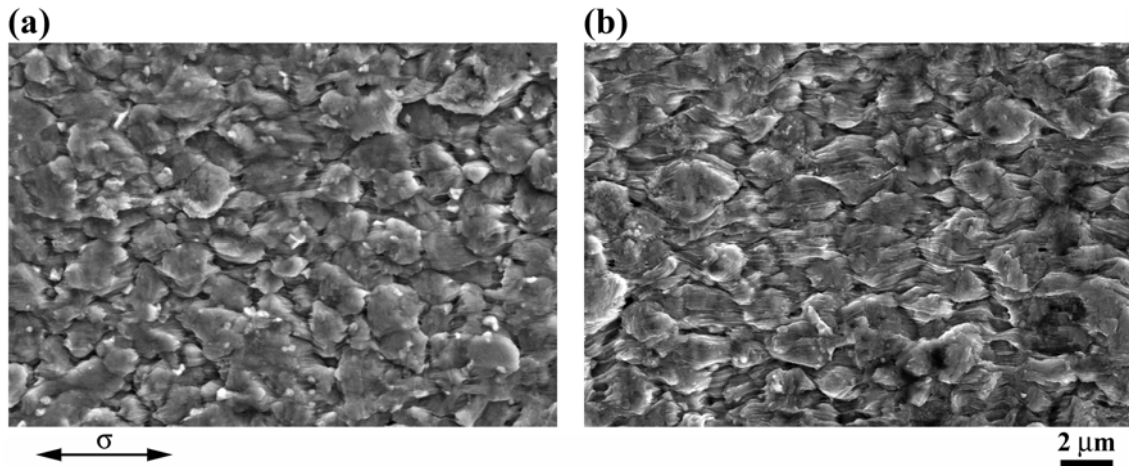
Figure 8. SEM micrographs showing the surface morphology in the gauge section after testing at an initial strain rate of 10^{-2} s^{-1}. (a) 3-passes sample tested at 300ºC and (b) 4-passes sample tested at 350ºC. Tensile axis is horizontal.

grain aspect ratio of the tested samples, close to one, do not account for the large elongations achieved, as it would do if a slip creep mechanism were operative during the tests. Additionally, the micrographs show crystallites emerging and moving apart with strings between them, which is characteristic of GBS.

Two SEM micrographs on the gauge section surface of the 3-passes sample after testing at 350ºC and at an initial strain rate of 10^{-2} s^{-1} are shown in Fig. 9. The topography of this tested sample still shows in most areas evidence of GBS (Fig. 9a). However, it is evident
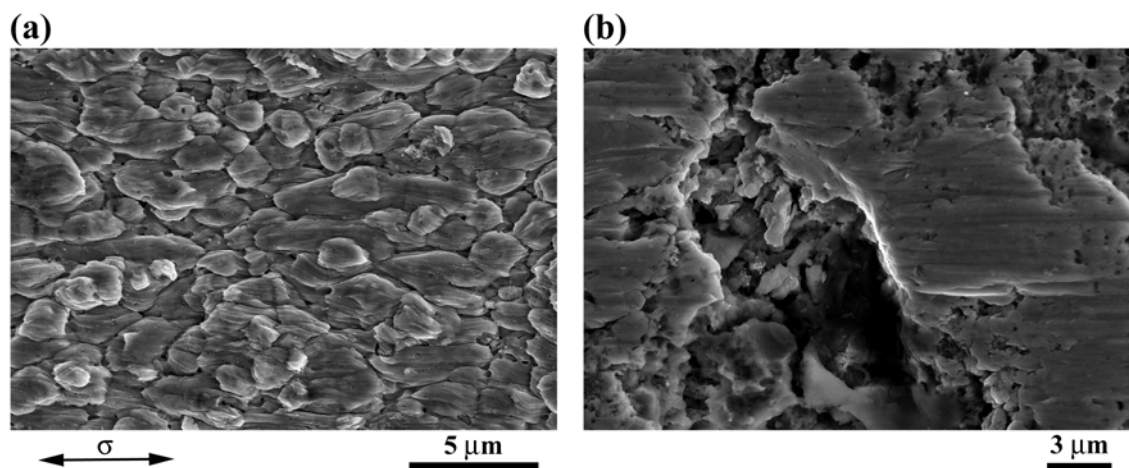

Figure 9. SEM micrographs showing the surface morphology in the gauge section of the 3-passes sample after testing at 350ºC and at an initial strain rate of 10^{-2} s^{-1}. (a) region I and (b) region II. Tensile axis is horizontal.

14

that, during the tensile tests at such conditions, the microstructure of the 3-passes sample not only coarsens, but elongates along the loading direction. Moreover, this tested sample exhibits, occasionally, excessively large grains (Fig. 9b), indicating a very heterogeneous structural coarsening, compatible with discontinuous recrystallization and abnormal grain growth.

XRD texture analysis was performed on the grip section of the same sample, that is, the 3-passes sample tested at 350ºC and at an initial strain rate of 10^{-2} s^{-1} (Fig. 10). The ODF reveals that texture is characterized by orientations along the β-fibre and orientations close to the former but shifted towards smaller φ_1 Euler angles, which are frequently subsumed as the R orientation. This is particularly evident in the sections φ_2= 0-45º, where the existing branch of β-fibre appears to split into two. However, it is also noticeable in the sections φ_2= 45-90º, especially in φ_2= 45º, where the maximum intensities of the texture are somewhat shifted from the ideal β-fibre orientations to smaller values of φ_1. The orientation shift from the rolling orientations towards the R orientation is a strong evidence for discontinuous
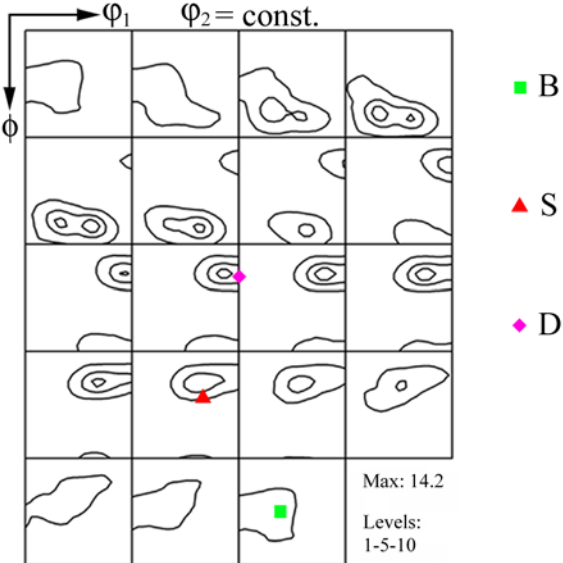

Figure 10. ODF on the grip section of the 3-passes sample after testing at 350ºC and at initial strain rate of 10^{-2} s^{-1}.

recrystalization in the grip section [31], which is consistent with the heterogeneous microstructure found in the gauge section of the same ARBed sample (Fig. 9). As the grip section is unaffected by deformation, these observations mean that the occurrence of discontinuous recrystallization in the 3-passes sample during testing at 350ºC is just a consequence of the high temperature. Note that 350ºC also corresponds to the processing temperature.

4. Discussion

The microstructure of the as-received material is characterized by pancake shaped grains of dimensions 60 x 47 x 4 μm^3. According to the TEM data (Fig. 2), the alloy microstructure becomes finer by the present ARB process, although d remains approximately constant at 440 nm with N. Microstructural examinations (Figs. 1 and 3) reveal that during the first three passes, the dislocation density decreases while the boundary definition increases with increasing N. However, further ARB passes, lead to a remarkable increase of the dislocation density and the presence of diffuse boundaries in relation to the 3-passes sample, which exhibit the maximum misorientation with $\theta = 30º$ (Fig. 4a). In addition, XRD texture analysis (Fig. 5) reveals that, during the ARB processing, the Al 7075 alloy develops the typical rolling β-fibre texture, whose intensity is maximum for the 3-passes sample. These observations are consistent with the occurrence of continuous recrystallization involving static and dynamic recovery up to N=3, but of discontinuous recrystallization for N > 3 that occurs during the inter-pass annealing stages as proved in Fig. 10.

Both recovery and discontinuous recrystallization require high temperature and are driven by the stored energy of the deformed state [32]. Recovery is a relatively homogeneous process in terms of both space and time. However, discontinuous recrystallization is a process involving the formation of new strain-free grains in certain parts of the specimen and

subsequent growth of these to consume the deformed or recovered microstructure. Therefore, discontinuous recrystallization is a phenomenon involving migration of grain boundaries, which can be reduced by particles exerting a force on them. This effect, determining the material thermal stability, is known as Zener drag and increases with increasing the pinning parameter $Z = 3F_vR/D$, where F_v is the volume fraction of particles, R is the mean grain radius and D is the mean particle diameter.

Two main types of particles were observed in the present 7075 Al alloy: Cr-rich dispersoids and Mg-Zn rich precipitates. Dispersoids remain almost unchanged during the ARB processing (Fig. 1). However, the Mg-Zn precipitates are remarkably larger in the ARB samples than in the starting material, being larger with increasing N. Consequently, the mean pinning effect of particles on the boundaries will be smaller with increasing N. This means that the thermal instability of the ARBed samples gradually increases with increasing N and, thus, the ease with which discontinuous recrystallization occurs during the inter-pass annealing stages also increases with increasing N. This will lead to an inhomogeneous microstructural evolution during the ARB processing.

The as-received material exhibits the typical recrystallization texture of non-shear banding Al-alloys, mainly characterized by a strong C orientation with RD-scatter [33]. As it is typical of rolling processes in aluminium [34], the present ARB process causes orientations to concentrate along a β-fibre, extending from the B to D orientation (Fig. 5). It is significant that the texture of the 3-passes sample after annealing at 350ºC is characterized by the R orientation, very close to the β-fibre (Fig. 10). Despite the absence of the C orientation, which has been reported as the recrystallization texture of aluminium in many investigations [35-40], this texture is indicative of discontinuous recrystallization during the annealing stage following the third pass. Indeed, some investigations [31,41-43] reveal that in the large strain regime the volume fraction of the R orientation after discontinuous recrystallization increases

with increasing strain at the expense of the C orientation. This can be interpreted by means of the oriented nucleation theory, which assumes that the preferred formation of some special orientations determines the final recrystallization texture [32,44], as explained below.

It is generally known that recrystallization nucleus form preferentially at deformation inhomogeneities [32,44], i.e. highly misoriented zones around large particles (> 1 μm), shear bands, transition bands or grain boundaries. At high strains, where the grain boundary area per unit volume and thus the number of nucleation sites is very high, nucleation at grain boundaries is largely favoured [45]. This takes place by the strain induced grain boundary migration (SIBM) mechanism [46], which involves the bulging of part of a pre-existing grain boundary, leaving a region behind the migrating boundary with lower dislocation content. So, the orientation of a grain boundary nucleus is likely to bear with some scatter the orientation of one of the two adjacent grains [47]. According to Fig. 5, up to N = 3, the fraction of grains with orientations along the β-fibre increases with increasing strain, while the fraction of grains with C orientation, which is only metastable upon rolling deformation, decreases with increasing strain in such a way that the presence of C orientation in the alloy after three ARB passes is negligible. The consequence is that, virtually, only grains with orientations close to the rolling orientations, frequently subsumed as the R-orientation, nucleate. This is probably the reason why, despite the occurrence of dynamic recrystallisation phenomena, the ARBed samples with more than three passes still exhibit the typical β-fibre texture (Fig. 5c).

According to the SEM examinations on the 3-passes sample after testing at 350ºC (Fig. 9), discontinuous recrystallization during the annealing stage after the third ARB pass gives rise to some large new grains in the alloy, which is consistent with the increment of d_{HAB} from N = 3 to N = 4 (Fig. 4b). Moreover, as a "fresh" substructure will be introduced in such large grains during the fourth pass, an increase of the dislocation density (Fig. 1) and of

the amount of boundaries with misorientation below 2º (Fig. 3) is also observed in the 4-passes sample with respect to the 3-passes sample.

The increment of the boundary misorientation and the reduction of the dislocation density from N = 4 to N = 5 (Figs. 1 and 3) appear to indicate that the alloy could resist discontinuous recrystallization during the annealing stage after the fourth pass. This can be ascribed to a remarkable reduction of the stored energy, and thus the driving force for recrystallization, during the previous annealing stage [30]. However, the microstructure of the 5-passes sample is still less recovered and misoriented than the 3-passes sample (Figs. 1 and 3). Moreover, the β-fibre of the 5-passes is still less intense than that of the 3-passes sample (Fig. 5c), equivalent to a lower rolling strain. This is a sign that, although the alloy manages to resist discontinuous recrystallization during some of the inter-pass annealing stages, the microstructure is actually destabilized from the third pass on and cannot recover this condition anymore. In fact, the increment of d_{HAB} from N = 5 to N = 6 (Fig. 4b) reveals that during the annealing stage after the fifth ARB pass the alloy is again affected by discontinuous recrystallization, preventing the attainment and hence the improvement of the excellent microstructural features corresponding to the 3-passes sample (Figs. 1 and 3).

The ARBed samples exhibit, at 300ºC and 350ºC, a mechanical behaviour characteristic of GBS at intermediate and high strain rates. First, the elongation to failure at 10^{-2} s^{-1} is much higher for the ARBed samples than for the as-received material (Fig. 6b). Second, the flow stress is at all the strain rates much lower for the ARBed samples than for the as-received material (Figs. 6a and 7). Finally, the stress exponents are much lower for the ARBed samples than for the as-received material (Fig. 7). In addition, the SEM examinations on the gauge section of the specimens tested at 300ºC and 350ºC and 10^{-2} s^{-1} (Figs. 8 and 9) show equiaxed grains emerging and sliding intensively, which are clear evidence of GBS, the mechanism responsible for superplasticity.

The constitutive relationships for GBS predict an improvement of superplastic properties with decreasing grain size [22]. It should be clarified that, since boundaries with low misorientation do not slide [21], the grain size from the point of view of superplasticity is determined by highly misoriented boundaries. Therefore, since the mean boundary misorientation angle exhibits a maximum for N = 3, optimum superplasticity would be expected for the 3-passes sample. Accordingly, at 300ºC, the best superplastic properties correspond to the 3-passes sample, which exhibits e_F= 140% at 10^{-2} s^{-1} (Fig. 6b). However, at 350ºC, the superplastic peak correspond to the 4-passes samples, exhibiting e_F= 185% at 10^{-2} s^{-1} (Fig. 6b). This can be rationalized considering that the microstructure obtained by the present ARB process is not the only factor which determines the superplastic potential of the alloy, but the stability of this microstructure at the testing temperature is of equal importance. In fact, as commented previously, the 3-passes sample is affected by discontinuous recrystallization at 350ºC (Figs. 9 and 10), while the 4-passes sample resists discontinuous recrystallization at this temperature (Fig. 8b).

Conclusions

The 7075 Al alloy was severely deformed at 350ºC by a 3:1 thickness reduction per pass accumulative roll bonding (ARB) process up to six passes. Characterization of microstructure, texture and mechanical properties makes possible to extract the following conclusions.

1. According to transmission electron microscopy examinations, a mean crystallite size around 440 nm is obtained for all the ARB passes. However, according to electron backscatter diffraction analysis, the mean boundary misorientation angle reaches a maximum of 30º, while the mean spacing of high angle boundaries (>15º) reaches a

minimum for the 3-passes sample. This can be ascribed to the occurrence of discontinuous recrystallization during the inter-pass annealing stages from the third pass onwards.

2. The gradual coarsening of the Mg-Zn precipitates during the ARB processing leads to an increment of the mean particle size in the ARBed samples in relation to the starting alloy. Consequently, the particle pinning effect diminishes, thus increasing thermal instability with the number of ARB passes.

3. Discontinuous recrystallization only induces a shift of the β-fibre toward smaller φ_1 Euler angles. For this reason, the ARBed samples are characterized by the β-fibre rolling texture, even after the third pass. The absence of cube orientation in the recrystallization textures, usually associated to discontinuous recrystallization in Al, indicates that nucleation takes place by the strain induced grain boundary migration mechanism, involving the bulging of part of a pre-existing grain boundary.

4. Tensile tests at 300ºC and 350ºC reveal that the operative deformation mechanism in the processed alloy is grain boundary sliding, characterized by a strong grain size dependence of stress, elevated elongation to failure and low stress exponent (n_{ap}). The strain rate for optimum superplasticity, determined by the region of the lowest n_{ap}, is between $3 \cdot 10^{-3}$ s^{-1} and 10^{-2} s^{-1}, sufficiently high for industrial application.

5. At 300ºC the maximum elongation to failure (e_F= 140%) is determined by the maximum boundary misorientation, corresponding to the 3-passes sample, as expected. At 350ºC, the maximum elongation to failure (e_F= 185%) is obtained for the 4-passes sample, attributable to a lower driving force for discontinuous recrystallization during annealing in comparison to the 3-passes sample.

Acknowledgements

References

[1] Y. Saito, N. Tsuji, H. Utsunomiya, T. Sakai, R.G. Hong, Scripta Mater. 9 (1998) 1221-1227.

[2] N. Tsuji, Y. Saito, S.-H. Lee, Y. Minamino, Adv. Eng. Mater. 5 (2003) 338-344.

[3] N. Tsuji, Y. Saito, H. Utsunomiya, S. Tanigawa, Scripta Mater. 40 (1999) 795-800.

[4] K.-T. Park, H.-J. Kwon, W.J. Kim, Y.-S. Kim, Mater. Sci. Eng. A (2001) 145-152.

[5] Z.P. Xing, S.B. Kang, H.W. Kim, J. Mater. Sci. 37 (2002) 717-722.

[6] X. Huang, N. Tsuji, N. Hansen, Y. Minamino, Mater. Sci. Eng. A 340 (2003) 265-271.

[7] M.T. Pérez-Prado, J.A. del Valle, O.A. Ruano, Scripta Mater. 51 (2004) 1093-1097.

[8] M. Karlík, P. Homola, M. Slámova, J. Alloy. Compd. 378 (2004) 322-325.

[9] M. Shaarbaf, M.R. Toroghinejad, Mater. Sci. Eng. A 473 (2008) 28-33.

[10] P. Hidalgo, C.M. Cepeda-Jiménez, O.A. Ruano, F. Carreño, Metall. Mater. Trans. A 41 (2010) 758-767.

[11] P. Hidalgo-Manrique, C.M. Cepeda-Jiménez, O.A. Ruano, F. Carreño, Mater. Sci. Eng. A 556 (2012) 287-294.

[12] P. Hidalgo-Manrique, C.M. Cepeda-Jiménez, A. Orozco-Caballero, O.A. Ruano, F. Carreño, J. Mater. Sci. 49 (2014) 833-841.

[13] I.J. Polmear, Light Alloys: Metallurgy of the Light Metals, third ed., Arnold, London, 1995.

[14] Kh. A.A. Hassan, A.F. Norman, D.A. Price, P.B. Prangnell, Acta Mater. 51 (2003) 1923-1936.

[15] S.G. Chowdhury, V.C. Srivastava, B. Ravikumar, S. Soren, Scripta Mater. 54 (2006) 1691-1696.

[16] S.G. Chowdhury, A. Dutta, B. Ravikumar, A. Kumar, Mater. Sci. Eng. A 428 (2006) 351-357.

[17] N. Takata, K. Yamada, K.-I. Ikeda, F. Yoshida, H. Nakashima, N. Tsuji, Mater. Trans. 48 (2007) 2043-2048.

[18] H. Pirgazi, A. Akbarzadeh, R. Petrov, J. Sidor, L. Kestens, Mater. Sci. Eng. A 492 (2008) 110-117.

[19] N. Kamikawa, N. Tsuji, Y. Minamino, Sci. Technol. Adv. Mat. 5 (2004) 163-172.

[20] A.J. Barnes, J. Mater. Sci. Eng. Perform. 16 (2007) 440-454.

[21] O. Ruano, O. Sherby, Rev. Metal. CENIM 19 (1983) 261-270.

[22] O.A. Ruano, O.D. Sherby, Rev. Phys. Appl. 23 (1988) 625-637.

[23] E. DiRusso, M. Conserva, M. Buratti, F. Gatto, Mater. Sci. Eng. 14 (1974) 23-26.

[24] J. Waldman, H. Sulinski, H. Markus, Metall. Trans. 5 (1974) 573-584.

[25] J.A. Wert, N.E. Paton, C.H. Hamilton, M.W. Mahoney, Metall. Trans. A 12 (1981) 1267-1276.

[26] N.E. Paton, C.H. Hamilton, J. Wert, M. Mahoney, J. Met. 34 (1982) 21-27.

[27] J. Xinggang, W. Qinglin, C. Jianzhong, M. Longxiang, J. Mater. Sci. 28 (1993) 6035-6039.

[28] J.M. García-Infanta, A.P. Zhilyaev, A. Sharafutdinov, O.A. Ruano, F. Carreño, J. Alloy. Compd. 473 (2009) 163-166.

[29] C.M. Cepeda-Jiménez, J.M. García-Infanta, O.A. Ruano, F. Carreño, J. Alloy. Compd. 509 (2011) 9589-9597.

[30] N. Kamikawa, N. Tsuji, X. Huang, N. Hansen, Acta Mater. 54 (2006) 3055-3066.

[31] O. Engler, H.E. Vatne, E. Nes, Mater. Sci. Eng. A 205 (1996) 187-198.

[32] F.J. Humphreys, M. Hatherly, Recrystallization and Related Annealing Phenomena, second ed., Elsevier, Oxford, 2004.

[33] O. Engler, Scripta Mater. 44 (2001) 229-236.

[34] J. Hirsch, K. Lücke, Acta Metall. 36 (1988) 2863-2882.

[35] K. Ito, R. Musick, K. Lücke, Acta Metall. 31 (1983) 2137-2149.

[36] J. Hirsch, K. Lücke, Acta Metall. 33 (1985) 1927-1938.

[37] A.L. Dons, E. Nes, Mater. Sci. Technol. 2 (1986) 8-18.

[38] J. Hirsch, E. Nes, K. Lücke, Acta Metall. 2 (1987) 427-438.

[39] D. Juul Jensen, Acta Metall. Mater. 43 (1995) 4117-4129.

[40] I. Samajdar, R.D. Doherty, Acta Mater. 46 (1998) 3145-3158.

[41] N. Hansen, D. Juul Jensen, Metall. Trans. A 17 (1986) 253-259.

[42] M.Z. Quadir, O. Al-Buhamad, L. Bassman, M. Ferry, Acta Mater. 55 (2007) 5438-5448.

[43] W.Q. Cao, A. Godfrey, N. Hansen, Q. Liu, Metall. Mater. Trans. A 40 (2009) 204-214.

[44] R.D. Doherty, D.A. Hughes, F.J. Humphreys, J.J. Jonas, D. Juul Jensen, M.E. Kassner, W.E. King, T.R. McNelley, H.J. McQueen, A.D. Rollet, Mater. Sci. Eng A 238 (1997) 219-274.

[45] M. Crumbach, M. Goerdeler, G. Gottstein, Acta Mater. 54 (2006) 3291-3306.

[46] P.A. Beck, P.R. Sperry, J. Appl. Phys. 21 (1950) 150-152.

[47] G. Gottstein, R. Sebald, J. Mater. Process. Techn. 117 (2001) 282-287.